JGR Solid Earth

RESEARCH ARTICLE
10.1029/2018JB015891

Predicting Homogeneous Bubble Nucleation in Rhyolite

Sahand Hajimirza[1], Helge M. Gonnermann[1], James E. Gardner[2], and Thomas Giachetti[3]

[1]Department of Earth, Environmental and Planetary Sciences, Rice University, Houston, TX, USA, [2]Jackson School of Geosciences, University of Texas at Austin, Austin, TX, USA, [3]Department of Earth Sciences, University of Oregon, Eugene, OR, USA

Key Points:
- Nucleation in rhyolitic decompression experiments at low supersaturations is decompression rate independent
- Nucleation at large supersaturations is controlled by decompression rate and occurs over a short timescale
- Surface tension of bubble nuclei deviates from surface tension of a planar interface as a function of the nucleus size

Correspondence to:
S. Hajimirza,
sahand@rice.edu

Citation:
Hajimirza, S., Gonnermann, H. M., Gardner, J. E., & Giachetti, T. (2019). Predicting homogeneous bubble nucleation in rhyolite. *Journal of Geophysical Research: Solid Earth*, *124*, 2395–2416. https://doi.org/10.1029/2018JB015891

Received 2 APR 2018
Accepted 29 JAN 2019
Accepted article online 1 FEB 2019
Published online 4 MAR 2019

Abstract Bubble nucleation is the critical first step during magma degassing. The resultant number density of bubbles provides a record of nucleation kinetics and underlying eruptive conditions. The rate of bubble nucleation is strongly dependent on the surface free energy associated with nucleus formation, making the use of bubble number density for the interpretation of eruptive conditions contingent upon a sound understanding of surface tension. Based on a suite of nucleation experiments with up to $>10^{16}$ bubbles per unit volume of melt, and using numerical simulations of bubble nucleation and growth during each experiment, we provide a new formulation for surface tension during homogeneous nucleation of H_2O bubbles in rhyolitic melt. It is based on the Tolman correction with a Tolman length of $\delta = 0.32$ nm, which implies an increase in surface tension of bubbles with decreasing nucleus size. Our model results indicate that experiments encompass two distinct nucleation regimes, distinguishable by the ratio of the characteristic diffusion time of water, τ_{diff}, to the decompression time, t_d. Experiments with $>10^{13}$ m^{-3} bubbles are characterized by $\tau_{diff}/t_d \ll 1$, wherein the nucleation rate predominantly depends on the interplay between decompression and diffusion rates. Nucleation occurs over a short time interval with nucleation rate peaks at high values. For experiments with comparatively low bubble number density the average distance between adjacent bubbles and the diffusion timescale is large. Consequently, $\tau_{diff}/t_d \gg 1$ and nucleation is nearly unaffected by diffusion and independent of decompression rate, with bubbles nucleating at an approximately constant rate until the sample is quenched.

1. Introduction

Bubbles in magma form when volatiles dissolved in silicate melt exsolve, because the solubility of many magmatic volatiles, such as water, is strongly pressure dependent. The resultant vesiculation produces bubbles that are composed of supercritical fluid, predominantly water, carbon dioxide, and other less abundant volatiles (e.g., Johnson et al., 1994; Murase & McBirney, 1973; Sparks, 1978; Wallace et al., 2015). Vesiculation includes bubble nucleation, growth, and also the loss of volatiles through flow of the exsolved volatiles within the permeable magma. The vesiculation process is of importance for volcanic eruptions, in part because the low density of the supercritical aqueous fluid phase inside bubbles imparts buoyancy to the magma (e.g., Wilson et al., 1980) and also because the fluid is highly compressible, thus bearing the potential to expand at high rates during magma ascent. Moreover, the viscosity of silica-rich melts increases by orders of magnitude when water exsolves, resulting in a feedback between pressure and vesiculation (e.g., Lensky et al., 2004; Prousevitch et al., 1993; Sparks, 1978).

Magma degassing therefore constitutes a rather complicated process with interplay between degassing and magma ascent. The first step, and necessary condition, for degassing is bubble nucleation. Nucleation is contingent upon the formation of clusters of volatile molecules that are of sufficient size to grow into bubbles (e.g., Abraham, 1974). Classical nucleation theory (CNT) quantifies the kinetics for the formation of such bubble nuclei. It allows for predictions of bubble nucleation rate, J, and resultant bubble number density, N_m, defined as the number of bubbles per unit volume of melt. In erupting magma, nucleation is driven by decompression that leads to volatile supersaturation of the melt (Sparks, 1978; Toramaru, 1989, 1990). At the same time, volatile diffusion into existing bubbles will limit the degree of supersaturation that can be achieved (e.g., Gonnermann & Manga, 2005, 2007; Prousevitch et al., 1993; Sparks, 1978). In other words, the nucleation process is controlled by an interplay between decompression and diffusion rates (e.g., Toramaru, 1989, 1995). As a consequence, bubble number density in erupted magmas provides information about the

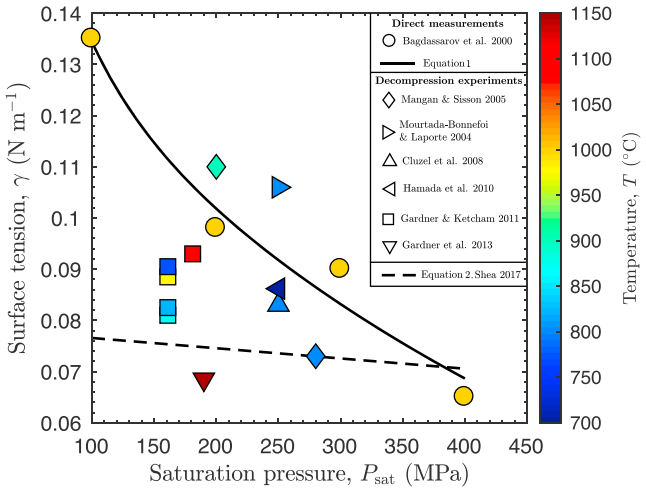

Figure 1. Surface tension of rhyolitic melt measured directly or estimated from nucleation experiments. Surface tension decreases somewhat with temperature and with increasing water saturation pressure.

kinetics of magma ascent, which in turn provides constraints on eruption dynamics and conditions that are not accessible to direct observation.

Measured bubble number densities in explosively erupted silicic magmas are high (10^{13}–10^{16} m^{-3}; e.g., Adams et al., 2006; Alfano et al., 2012; Carey et al., 2009; Giachetti et al., 2010; Gurioli et al., 2005; Houghton et al., 2010; Klug & Cashman, 1994; Klug et al., 2002; Piochi et al., 2008; Polacci, 2005; Toramaru, 1990). Based on homogeneous bubble nucleation experiments, wherein bubbles nucleate in the bulk melt phase, such high bubble number densities are thought to require supersaturation pressures of ≥100 MPa (Fiege & Cichy, 2015; Gardner & Ketcham, 2011; Gondé et al., 2011; Hurwitz & Navon, 1994; Mangan & Sisson, 2000; Marziano et al., 2007; Mourtada-Bonnefoi & Laporte, 1999, 2002 ; Nowak et al., 2011; Preuss et al., 2016) and decompression rates of ∼100 MPa/s (Hamada et al., 2010; Massol & Koyaguchi, 2005; Mourtada-Bonnefoi & Laporte, 2004; Toramaru, 1989, 1995, 2006). During heterogeneous nucleation preferential nucleation sites, such as Fe-Ti oxide crystals, may reduce the energy of nucleus formation. Consequently, it has been proposed that abundant oxides, or heterogeneities in melt structure that are too small to be detected, may play an important role in facilitating the high nucleation rates required to produce the bubble number densities measured in explosively erupted silicic magmas (Shea, 2017). The implication is that homogeneous bubble nucleation experiments might lack these heterogeneous nucleation sites and therefore lead to overestimates on supersaturation and/or decompression rates. However, given the lack of direct observational evidence for heterogeneous nucleation sites, at number densities of up to ∼ 10^{16} m^{-3}, and given that heterogeneous nucleation rate can be calculated by scaling surface tension based on homogeneous nucleation (e.g., Cluzel et al., 2008), the prediction of bubble nucleation must be rooted in a sound understanding of homogeneous nucleation. A necessary first step in interpreting vesicle data of volcanic products is therefore the ability to reliably predict homogeneous nucleation during experiments under known conditions. This is the objective of our study. By improving the capability to model homogeneous bubble nucleation in rhyolitic melts, across a wide range of decompression rates and volatile saturations, we aim to provide an improved foundation for investigating bubble nucleation during volcanic eruptions, including the possibility of heterogeneous nucleation.

2. Review of Surface Tension (γ) in Rhyolite

CNT is based on the free energy associated with the formation of bubble nuclei. It is the sum of the negative bulk energy and positive surface energy. The latter derives from the surface free energy per unit surface area of the nucleus or, equivalently, the surface tension between bubble nucleus and melt. It is usually assumed that surface tension during nucleation equals the macroscopically measurable value. This is called the capillary approximation. The macroscopic value of surface tension has been measured directly in silicate melts using methods such as sessile drop or pin detachment (Murase & McBirney, 1973; Taniguchi, 1988; Walker & Mullins, 1981). For hydrous silicate melts direct surface tension measurements are limited to three studies: Khitarov et al. (1979) for basaltic melt, Epel'baum (1973) for rhyodacite melt, and Bagdassarov et al. (2000) for haplogranitic melt. Of these three, the results of Bagdassarov et al. (2000) are frequently used for the prediction of bubble nucleation. Bagdassarov et al. (2000) found that γ_B increases somewhat with temperature and that it decreases with water saturation (Figure 1). Independent regression of their data results in the empirical formula:

$$\begin{aligned}\gamma_B = {} & 1.21\times10^{-1}\exp(-2.24\times10^{-2}P_{sat}) \\ & + 1.47\times10^{-1}\exp(-1.90\times10^{-3}P_{sat}) \\ & + 7.5\times10^{-5}(T-1,000).\end{aligned} \quad (1)$$

The subscript B indicates the macroscopic surface tension of Bagdassarov et al. (2000). T is temperature in degrees Celsius, and P_{sat}, the saturation pressure in units of megapascals, is the fictive pressure at which melt would be saturated with H_2O (see Table 1 for symbol definitions and units).

Table 1
Definition of Symbols

Symbol	Definition
a_0	Average distance between two neighboring water molecules (m)
C_m	Water concentration in melt
C_i	Initial water concentration in melt
C_R	Water concentration at fluid-melt interface
D	Diffusivity (m^2/s)
$F(R, t)$	Size distribution function of bubbles (number per volume of melt)
f	Fugacity coefficient of water
J	Nucleation rate ($m^{-3}{\cdot}s^{-1}$)
k_B	The Boltzmann constant (J/K)
l	Average diffusion length between bubbles (m)
M_w	The molar mass of water (kg/mol)
M_k	kth moment of bubble size distribution (m^k per volume of melt)
M_0	Zeroth moment, bubble number density (number per volume of melt)
M_1	First moment, radius of bubbles (m per volume of melt)
M_2	Second moment, surface area of bubbles (m^2 per volume of melt)
M_3	Third moment, volume of bubbles (m^3 per volume of melt)
m_b	Average mass of bubbles (kg)
m_c	Mass of critical nucleus (kg)
m_g	Total mass of fluid phase (kg per volume of melt)
N_A	The Avogadro's number (mol^{-1})
N_m	Observed bubble number density in the experiments (number per volume of melt)
N_m^*	Predicted bubble number density by the model (number per volume of melt)
$n(R_c)$	Equilibrium number density of critical nuclei (number per volume of melt)
n_0	Concentration of water molecules in the melt (number per volume of melt)
P	Pressure (Pa)
P_m	Melt pressure (Pa)
P_n	Pressure inside a critical nucleus (Pa)
P_i	Initial pressure in experiments (Pa)
P_f	Final pressure in experiments (Pa)
P_{sat}	Saturation pressure of water (Pa)
P_b	Average pressure inside bubbles (Pa)
q	diffusive mass flux of water into bubbles ($m^{-2}{\cdot}s^{-1}$)
R	Bubble radius (m)
$\bar{R}$	Mean bubble radius (m)
R_c	Critical bubble radius (m)
R_e	Radius of equimolar dividing surface (m)
R_s	Radius of surface of tension (m)

Using the macroscopic surface tension in CNT neglects a potential dependence of surface tension on nucleus size, hypothesized to be the main reason for large discrepancies in nucleation kinetics between CNT and experiments (Debenedetti, 1996; Lubetkin, 2003; Navon & Lyakhovsky, 1998). The difference in surface tension between a planar interface and a curved one, with radii of curvature less than ~10 nm, is thought to be significant (Fisher & Israelachvili, 1981; Joswiak et al., 2013; Tolman, 1949). The surface tension of a bubble nucleus is, however, impossible to measure directly because of the small size of bubble nuclei and because nucleation in silicate melts occurs at high pressures and temperatures. Furthermore, bubble nuclei are ephemeral and grow rapidly in size. Instead, surface tension has to be estimated from bubble nucleation experiments wherein volatile-saturated melt is decompressed at some rate to a lower value at which the sample is quenched. Within the interior of the quenched sample the bubble number density is determined

Table 1 (*continued*)

Symbol	Definition
RMSE	Root-mean-square error (number per volume of melt)
$[SiO_2]$	Silica content (wt %)
T	Temperature (K)
t	Time (s)
t_d	Decompression time (s)
t_{peak}	Time at which nucleation rate is maximum (s)
t_{post}	Time at which sample was stayed at final pressure (s)
t_{quench}	Time from onset of decompression until quench (s)
W_n	Change in free energy due to formation of a critical nucleus (J)
W_n^*	Empirical nucleation energy (J)
Z	Zeldovich factor
α	Surface tension correction
Γ	Excess superficial molar concentration (mol/m^2)
γ	Surface tension of melt-fluid interface (N/m^2)
γ_B	Surface tension measured by Bagdassarov et al. (2000) (N/m^2)
γ_∞	Surface tension of melt-fluid planar interface (N/m^2)
ΔP_{ss}	Supersaturation pressure (Pa)
δ	Tolman length (m)
η	Melt viscosity (Pa s)
ρ_m	Melt density (kg/m^3)
ϵ	molar concentration of H_2O at the melt-fluid interface (mol/m^3)
τ_{diff}	Diffusion timescale (s)
ϕ	Volume fraction of fluid phase (m^3 per volume of melt)
Ω	Molecular volume of water (mol/m^3)
ω	Growth frequency of a critical nucleus (s^{-1})

Note. The provided units are used for variables in the equations unless otherwise is stated in the text.

from thin sections or microtomographic reconstructions. A time-averaged nucleation rate is then estimated from the ratio of bubble number density and the time over which the sample was decompressed. Examples of such experiments in rhyolite are by Gardner and Ketcham (2011), Gardner et al. (2013), and Mangan and Sisson (2005), and their results are included in Figure 1. From this time-averaged nucleation rate a surface tension is calculated using CNT. This approach implicitly assumes a constant nucleation rate over the duration of the experiment, which is unlikely to be the case. Alternatively, surface tension can be estimated by taking advantage of the time for the onset of nucleation, which is the minimum time required for bubbles to be observable in a sample of given size. In this case samples are decompressed from the same initial pressure to different final pressures until bubbles are first observed within the sample. The evolution of N_m is calculated by integrating J with different values of surface tension to find the value of surface tension that matches the minimum supersaturation pressure at which bubbles are experimentally observable. Examples of such experiments in rhyolite are by Mourtada-Bonnefoi and Laporte (2004) and Hamada et al. (2010); their results are also shown in Figure 1. Either approach yields constant surface tension estimates, but neither accounts for a potential dependence on nucleus size or the evolving physical properties of the system. In addition, a source of inconsistency among existing estimates is the choice of parameter values (such as molecular volume of water, diffusivity, and the use of saturation pressure or nucleus pressure; e.g., Cluzel et al., 2008; Hamada et al., 2010; Shea, 2017). This inconsistency motivated Shea (2017) to recalculate and fit surface tension from existing bubble nucleation experiments, resulting in

$$\begin{aligned}\gamma = {} & 6\times10^{-2}\ \exp(2.2\times10^{-2}(SiO_2 - 66.5)) \\ & - 2\times10^{-5}(P_{sat} - 200) \\ & + 5\times10^{-6}(T - 900),\end{aligned} \tag{2}$$

and also shown in Figure 1. Here SiO_2 is silica content in units of weight percent, P_{sat} in units of megapascals, and T is in units of degrees Celsius.

Here we report a comprehensive suite of homogeneous bubble nucleation experiments in rhyolitic melt that were performed under consistent experimental conditions of pressure, temperature, and water concentration. Using the sole direct measurements of surface tension in silicic melt by Bagdassarov et al. (2000) as a starting point, we develop a functional form for surface tension that enables the simulation of bubble nucleation across the full range of saturation conditions and decompression rates. We account for the effect of nucleus size through a Tolman correction (Joswiak et al., 2013; Lubetkin, 2003; Schmelzer & Baidakov, 2016; Tolman, 1949), which has been shown to improve the agreement between predicted and observed nucleation rates (Joswiak et al., 2013). The Tolman correction defines the ratio of the size-dependent surface tension of the bubble nucleus, $\gamma(R_s)$, to the surface tension of a planar surface with infinite radius of curvature and therefore denoted as γ_∞. The Tolman correction is defined as (Tolman, 1949)

$$\frac{\gamma(R_s)}{\gamma_\infty} = \frac{1}{1 + 2\delta/R_s}. \tag{3}$$

Here R_s is radius of the surface of tension and δ is called the Tolman length. Both parameters are described in section 7. We assume that γ_∞ can be approximated by macroscopic measured values, that is the water-dependent surface tension of Bagdassarov et al. (2000), albeit with a correction to account for differences in melt composition between Bagdassarov et al.'s (2000) haplogranite and our rhyolitic samples, as well as other potentially unaccounted discrepancies. Because there are no priori constraints on the form of this correction, we assume that it scales linearly with γ_B and define $\gamma_\infty = (1 + \alpha)\gamma_B$, where α is an empirical constant.

3. Review of CNT

CNT quantifies the statistical rate of formation of nuclei of critical radius as a result of random fluctuations of volatile molecules (e.g., Abraham, 1974; Debenedetti, 1996). It defines the steady state nucleation rate as

$$J = \omega(R_c)\ Z\ n(R_c), \tag{4}$$

where $\omega(R_c)$ is the frequency at which single water molecules enter the critical nuclei, R_c is the radius of a critical nucleus, Z is the Zeldovich correction factor, which corrects for the departure of number density of critical nuclei from the equilibrium value, and $n(R_c)$ is the equilibrium number density of critical nuclei. For bubble nucleation in a multicomponent system ω is defined as (Hurwitz & Navon, 1994; Hirth et al., 1970)

$$\omega = \left(4\pi R_c^2\right)\frac{n_0 D}{a_0}, \tag{5}$$

where D is the diffusivity of water molecules within the melt and $a_0 \approx n_0^{-1/3}$ is an average distance between the centers of two neighboring water molecules, with n_0 the concentration of water molecules in the melt. The latter is

$$n_0 = \frac{C_m \rho_m N_A}{M_w}, \tag{6}$$

where C_m is water concentration (molecular and hydroxyl), ρ_m is melt density, N_A is the Avogadro's number, and M_w is the molar mass of water. The radius of the critical nucleus, R_c, is estimated from the Young-Laplace capillary relation:

$$R_c = \frac{2\gamma}{P_n - P_m}, \tag{7}$$

where P_n is the pressure inside the critical nucleus and P_m is the melt pressure. P_n is related to P_{sat} through (Cluzel et al., 2008)

$$f(P_n, T)P_n = f(P_{sat}, T)P_{sat}e^{\Omega(P_m - P_{sat})/k_B T}, \tag{8}$$

where $f(P, T)$ is the fugacity coefficient of water at the given pressure and temperature, Ω is the molecular volume of water, T is absolute temperature at nucleation in kelvins, and $k_B = 1.38 \times 10^{-23}$J/K is the Boltzmann constant. Nuclei smaller than R_c will be unable to persist and grow in size. The equilibrium number

density of critical nuclei, $n(R_c)$, is proportional to the exponential of the reversible work needed to form a critical nucleus:

$$n(R_c) = n_0 \exp\left(-\frac{W_n}{k_B T}\right), \tag{9}$$

where W_n is the change in free energy required to form a new interface between a nucleus and surrounding phase. It was first derived by Gibbs (1961) and is given by

$$W_n = \frac{16\pi\gamma^3}{3(P_n - P_m)^2}. \tag{10}$$

Lastly, a simplified Zeldoich correction factor Z for bubble nucleation in a multicomponent silicate melt is derived by Hurwitz and Navon (1994) as

$$Z = \frac{\Omega(P_n - P_m)^2}{8\pi\gamma^{3/2}\sqrt{k_B T}}. \tag{11}$$

By substituting equations (5), (9), and (11) into equation (4) the classical homogeneous steady state nucleation rate can be calculated as

$$J = \frac{2\Omega n_0^2 D}{a_0}\sqrt{\frac{\gamma}{k_B T}}\exp\left(-\frac{16\pi\gamma^3}{3k_B T(P_n - P_m)^2}\right). \tag{12}$$

Because there currently are no established experimental constraints on the time lag of nucleation or the induction time (e.g., Schmelzer et al., 2017), during the nucleation of water bubbles in rhyolitic melt, we will assume throughout that nucleation is at steady state in experiments and model simulations.

4. Experimental Methods

For experiments, we used cylinders of 2.2 mm in diameter and 1.1–1.3 cm in length, cored from a high silica rhyolitic obsidian with less than 1 vol. % of Fe-Ti oxide microlites observed in thin section of several cores. The glass composition, determined by electron microprobe and normalized to 100 wt %, was 76.53 SiO_2, 0.06 TiO_2, 13.01 Al_2O_3, 0.79 FeO, 0.08 MnO, 0.02 MgO, 0.74 CaO, 3.87 Na_2O, and 4.91 K_2O (Gonnermann & Gardner, 2013). All sharp edges of the glass were ground using emery paper and washed, in order to avoid piercing of metal tubing in which they were held during the experiments. Experiments were carried out in two steps: Each sample was first hydrated at pressure P_i and temperature T (Table 2) and thereafter decompressed to final pressure P_f (Table 3).

During the hydration step the obsidian sample, together with sufficient distilled water to saturate the melt (usually 10% by weight of the cylinder), were placed in a 4-mm outer diameter Au capsule. The capsule was crimped, welded shut, and weighed before and after it was heated to check for leaks. The capsule was then placed inside an externally heated cold-seal pressure vessel, made of a Nickel-based alloy, and held at P_i and T for at least 5 days (Table 2). Hydration at 850–875 °C, produced crystal free hydrated melt, which ensures homogeneous bubble nucleation during decompression (Gardner et al., 1999). The sample was then quenched and split into at least two parts. One part was used to measure the concentration of dissolved water using a Thermo Electron Nicolet 6700 spectrometer and a Continuum infrared microscope. Water concentrations are listed in Table 2 as the averaged sum of molecular water and hydroxyls, determined from absorbances at 5,250 and 4,500 cm^{-1}, using a white-light source, a CaF_2 beamsplitter, and the model of Zhang et al. (1997). The thickness of the sample, at the location where each spectrum was collected, was measured using a Heidenhain focus drive linear encoder. Repeated measurements indicated that it was precise to $\pm 0.6\mu$m. The other part(s) of each sample was (were) used for the decompression steps.

In the decompression step the hydrated sample was sealed inside an Au capsule and placed into a cup, located on the end of an Inocel rod. The rod was then inserted into an externally heated rapid-quench cold-seal pressure vessel. The pressure vessel was heated to the desired temperature, and the sample was raised into the hot zone of the pressure vessel by an external magnet. Pressure was quickly adjusted by a hand-operated intensifier to 1 MPa above P_i to prevent exsolution of water. After the sample had been heated for 5 min, pressure was released to the final pressure over a time interval, t_d. The sample was then held at P_f for a duration of t_{post}. Finally, it was quenched at a rate of approximately 150 K/s by lowering it back into the

Table 2
List of Hydration Experiments

Hydration	P_i (MPa)	t_h (hr)	T (°C)	$[H_2O]$ (wt%)
G-591[a,b]	160	120	875	5.01 ± 0.18
G-630[a,b]	160	120	875	4.81 ± 0.14
G-695[a,b]	160	120	875	4.95 ± 0.05
G-610[a,b]	160	120	875	5.00 ± 0.03
G-931[a,b]	160	120	875	5.03 ± 0.02
G-594[a,b]	160	120	875	5.17 ± 0.50
G-644[a,b]	160	120	875	4.90 ± 0.08
G-882[a,b]	160	120	875	5.03 ± 0.01
G-883[a,b]	160	120	875	4.93 ± 0.05
G-885[a,b]	160	120	875	5.00 ± 0.01
G-595[a,b]	160	120	875	4.93 ± 0.13
G-1594A	160	118	875	4.79 ± 0.01
G-1607	160	121	875	4.85 ± 0.08
G-876[a,b]	160	120	875	5.08 ± 0.01
G-1570	190	168	850	5.70 ± 0.01
G-1594B	200	118	875	5.51 ± 0.03
G-1608	200	123	875	5.48 ± 0.04
G-1121[b]	200	120	875	5.62 ± 0.06
G-1140[b]	200	120	875	5.66 ± 0.02
G-1147[b]	200	120	875	5.52 ± 0.02
G-1457	200	144	850	5.71 ± 0.02
G-1456	200	145	850	5.70 ± 0.01
G-1483	200	216	850	5.50 ± 0.08
G-1608	200	123	850	5.48 ± 0.04
G-1448	200	167	850	5.70 ± 0.01
G-1544[c]	220	150	850	5.68 ± 0.01
G-1545[c]	220	150	850	5.59 ± 0.04
G-1590[c]	250	167	850	6.29 ± 0.01
G-1591[c]	250	167	850	6.29 ± 0.02
G-1680[c]	250	167	850	6.45 ± 0.08
G-1477	250	185	850	6.23 ± 0.01
G-1451	250	187	850	6.35 ± 0.05
G-1446	250	197	850	6.28 ± 0.01
G-1455	250	143	850	6.23 ± 0.03

Note. P_i is saturation pressure, t_h is total hydration duration, T is temperature during hydration, and $[H_2O]$ is the concentration of dissolved water.
[a]Experiments discussed in Gardner and Ketcham (2011). [b]Experiments discussed in Gonnermann and Gardner (2013). [c]Experiments discussed in Gardner et al. (2018).

water-cooled jacket. Using diffusion modeling, we have confirmed that bubble resorption during quenching has a negligible effect on N_m and R (Gardner et al., 2018). The sample was weighed to check for any water loss and then sectioned to estimate bubble number density, N_m, defined as number of bubbles nucleated within the interior of the sample per volume of glass.

Two different methods were used to measure N_m. For samples in which relatively few bubbles nucleated, N_m was measured by counting all bubbles that appeared in several regions of the sample, each 40 μm × 40 μm in surface area, as the field of view was moved through the sample using the focusing knob of the microscope. The depth of view was usually between 800 and 2,000 μm, as measured using the focus drive encoder. Bubble

Table 3
List of Decompression Experiments

Run	Hydration	P_i (MPa)	P_f (MPa)	t_d (s)	t_p (s)	T (°C)	$W_n^*(\gamma_b)$ (10^{-18} J)	$W_n^*(\gamma)$ (10^{-18} J)	N_m (m^{-3})	ϕ (%)	τ_{diff}/t_d
G-660[a,b]	G-630	161	80	5.0	55	875	6.5	1.8	0		—
G-593[a,b]	G-591	161	65	3.0	57	875	4.5	1.4	0	—	—
G-724[a,b,c]	G-695	161	52.5	10.0	50	875	3.5	1.2	2.50×10^{8}	—	5.8×10^{3}
G-906[a,b,c]	G-883	161	51.5	10.0	50	825	3.2	1.2	0	—	—
G-658[a,b]	G-610	161	47.0	8.0	52	875	3.2	1.2	4.76×10^{8}	—	4.6×10^{3}
G-938[a,b]	G-931	161	37.0	10.0	50	825	2.5	1.0	73.5×10^{8}	—	3.8×10^{3}
G-604[a,b]	G-594	161	33.0	20.0	40	875	2.5	1.0	2.91×10^{9}	—	5.3×10^{2}
G-665[a,b]	G-644	161	22.5	9.0	51	875	2.1	0.1	2.14×10^{9}	—	1.5×10^{3}
G-890[a,b]	G-882	161	22.0	10.0	60	825	2.0	0.9	2.26×10^{9}	—	1.8×10^{3}
G-907[a,b]	G-885	161	15.0	16.0	44	825	1.7	0.9	4.95×10^{8}	—	3.1×10^{3}
G-608[a,b]	G-595	161	13.5	11.0	109	875	1.8	0.9	3.21×10^{10}	—	2.1×10^{2}
G-1614	G-1594A	161	13.0	9.48	0	875	1.8	0.9	1.05×10^{9}	—	2.3×10^{3}
G-1627	G-1607	161	13.0	15.7	18.1	875	1.8	0.9	1.10×10^{10}	—	2.9×10^{2}
G-1616	G-1594A	161	11.0	15.5	5.3	875	1.8	0.9	1.09×10^{9}	—	1.4×10^{3}
G-1628	G-1607	161	11.0	10.8	28.87	875	1.8	0.9	2.7×10^{10}	—	2.3×10^{2}
G-889[a,b]	G-876	161	8.5	10.0	50	825	1.6	0.8	7.84×10^{10}	—	1.7×10^{2}
G-1592[c,d]	G-1570	191	77	2.27	58	850	2.9	1.1	1.86×10^{11}	0.8	2.9×10^{2}
G-1593[d]	G-1570	191	52	3.11	57	850	1.9	0.9	5.89×10^{11}	12.3	9.7×10^{1}
G-1129[b]	G-1129	201	100	17.0	43	875	3.8	1.2	—	—	—
G-1159[b]	G-1147	201	85.5	10.0	48	875	2.8	1.1	—	—	—
G-1617	G-1594B	201	75.5	45.46	0	875	2.4	1.0	1.01×10^{8}	—	1.8×10^{3}
G-1622	G-1594B	201	75.0	33.80	29.5	875	2.4	1.0	1.38×10^{9}	—	4.4×10^{2}
G-1632	G-1608	201	75.0	33.92	56.5	875	2.4	1.0	2.31×10^{10}	—	6.5×10^{1}
G-1148[b]	G-1140	201	74.5	35.0	25.0	875	2.4	1.0	5.93×10^{9}	—	1.5×10^{2}
G-1620	G-1594B	201	74.2	27.7	12.1	875	2.3	1.0	8.0×10^{8}	—	7.7×10^{2}
G-1482[d]	G-1457	201	54.0	1.46	60.0	850	1.6	0.8	2.57×10^{12}	31.8	7.5×10^{1}
G-1481[d]	G-1457	201	54.0	2.30	14.6	850	1.6	0.8	1.23×10^{12}	2.6	7.8×10^{1}
G-1484[d]	G-1456	201	54.0	1.65	89.8	850	1.6	0.8	3.39×10^{12}	33.1	5.6×10^{1}
G-1501[d]	G-1483	201	54.0	1.43	31.2	850	1.6	0.8	2.63×10^{12}	25.9	7.9×10^{1}
G-1638[d]	G-1608	201	42.0	7.65	52.5	875	1.4	0.8	5.89×10^{13}	51.4	1.6×10^{0}
G-1466[d]	G-1448	201	29.5	3.40	15.0	850	1.2	0.7	5.89×10^{14}	73.6	8.9×10^{-1}
G-1480[d]	G-1456	201	29.0	2.18	61.1	850	1.2	0.7	1.86×10^{15}	61.1	6.3×10^{-1}
G-1500[d]	G-1483	201	29.0	1.58	90.6	850	1.2	0.7	3.16×10^{15}	60.5	6.3×10^{-1}
G-1510[d]	G-1483	201	28.5	1.14	45.2	850	1.1	0.7	2.82×10^{15}	62.9	9.4×10^{-1}
G-1470[d]	G-1448	201	28.5	2.16	9.3	850	1.1	0.7	1.74×10^{15}	58.8	6.8×10^{-1}
G-1581[d]	G-1544	221	57.0	1.52	13	850	1.2	0.7	6.03×10^{15}	44.1	4.8×10^{-1}
G-1582[d]	G-1544	221	56.0	1.99	58	850	1.2	0.7	2.69×10^{15}	31.6	6.1×10^{-1}
G-1585[d]	G-1544	221	52.0	1.46	29	850	1.2	0.7	5.37×10^{15}	41.9	5.3×10^{-1}
G-1586[d]	G-1545	221	49.0	2.11	58	850	1.1	0.7	2.51×10^{15}	38.3	6.1×10^{-1}
G-1587[d]	G-1545	221	46.0	1.76	58	850	1.1	0.7	3.89×10^{15}	32.2	5.5×10^{-1}
G-1636[e]	G-1590	251	200.0	1.4	58.6	850	14.4	2.9	0	—	—

Table 3 (*continued*)

Run	Hydration	P_i (MPa)	P_f (MPa)	t_d (s)	t_p (s)	T (°C)	$W_n(\gamma_b)$ (10^{-18} J)	$W_n(\gamma)$ (10^{-18} J)	N_m (m^{-3})	ϕ (%)	τ_{diff}/t_d
G-1639[e]	G-1591	251	180.0	1.8	58.2	850	7.2	1.7	0	—	—
G-1611[e]	G-1590	251	173.5	2.0	58	850	6.0	1.5	0	—	—
G-1645[e]	G-1591	251	149.0	1.9	58.1	850	3.4	1.1	0	—	—
G-1609[c,e]	G-1590	251	149.0	2.37	57	850	3.4	1.1	2.75×10^9	—	4.9×10^3
G-1685[e]	G-1680	251	134.0	1.71	58	850	2.5	0.9	2.09×10^9	—	8.1×10^3
G-1523[e]	G-1477	251	122.0	1.87	90	850	2.0	0.8	8.71×10^{11}	4.2	1.3×10^2
G-1502[d]	G-1451	251	98.0	1.14	17	850	1.4	0.7	6.61×10^{15}	14.1	5.6×10^{-1}
G-1503[d]	G-1477	251	98.0	1.57	61	850	1.4	0.7	1.41×10^{15}	22.7	1.1×10^0
G-1513[d]	G-1477	251	97.0	1.68	90	850	1.4	0.7	6.17×10^{14}	17.9	1.9×10^0
G-1485[d]	G-1451	251	76.0	1.96	15	850	1.0	0.6	2.69×10^{16}	28.6	1.3×10^{-1}
G-1473[d]	G-1446	251	40.0	2.57	30	850	0.7	0.6	1.51×10^{16}	49.3	1.4×10^{-1}
G-1471[d]	G-1455	251	39.0	1.45	6	850	0.7	0.5	9.12×10^{15}	44.9	3.6×10^{-1}
G-1476[d]	G-1446	251	39.0	1.17	90	850	0.7	0.5	1.35×10^{16}	50.1	1.8×10^{-1}

Note. P_i is initial pressure, P_f is final pressure, t_d is decompression time, t_p is hold time at P_f before quench, T is temperature, $W_n(\gamma_b)$, and $W_n(\gamma)$ are nucleation energy estimated using surface tension from Bagdassarov et al. (2000) and the one found in this study, respectively. N_m is bubble number density, ϕ is volume fraction of bubbles, and τ_{diff}/t_d is the ratio of diffusion timescale over decompression timescale.
[a]Experiments discussed in Gardner and Ketcham (2011). [b]Experiments discussed in Gonnermann and Gardner (2013). [c]Experiments that are considered as outliers. [d]N_m was determined by scanning electron microscope analysis, whereas all other samples used an optical microscope. [e]Experiments discussed in Gardner et al. (2018).

number densities in each region were then estimated by dividing the number of bubbles counted by the corresponding volume of melt. The individual values obtained were averaged to give the final value of N_m.

In samples where bubbles were too numerous to be counted individually, N_m was estimated using images obtained at four different areas of thin section of the sample. The grayscale images were taken using a scanning electron microscope at a single resolution of 0.91 to 0.09 μm (pixel)$^{-1}$, depending on the size of bubbles. For four samples the images were randomly chosen from the stack of images taken at a resolution of 4 μm (pixel)$^{-3}$ at the University of Texas High-Resolution X-ray Computed Tomography Facility. Each image was transformed to binary using Adobe Photoshop®. The two-dimensional bubble number density was then estimated in each image by counting the number of individual bubbles and the surface area of glass using the Image Processing Toolbox of MATLAB®. N_m was then obtained from the two-dimensional bubble number density using the method developed by Sahagian and Proussevitch (1998). The final N_m of the sample was estimated by taking the average N_m of the four images analyzed. See Giachetti et al. (2019) for more details on analyzing experiments with high N_m. In both methods bubbles that appear to consist of two or more partially coalesced bubbles were counted separately as individual bubbles.

5. Numerical Model

5.1. Conceptual Model

We used a numerical model to calculate the evolution of bubble number density and bubble size during each experiment. The model constitutes a system of coupled ordinary differential equations that describe the rate of change in the number of bubbles per unit volume of melt during decompression at some given rate. The model is isothermal because the pressurizing medium in our experiments was water, and, unlike for experiments pressurized by compressed gas (e.g., Hamada et al., 2010), changes in temperature associated with decompression or volatile exsolution were not large enough to significantly affect the water solubility or melt viscosity in our experiments (Gonnermann & Gardner, 2013). The independent variable is time, t. The dependent variables are the zeroth through third moments of the bubble population, Indicative of bubble number density (N_m^*), mean bubble radius ($\bar{R}$), surface area of bubbles, and volume fraction of bubbles (ϕ), respectively. The concentration of dissolved H_2O in the melt, C_m, is the fifth dependent variable. Any changes in the dependent variables are driven by the change in external pressure, P_m, which is a prescribed variable. The model is thus meant to simulate the conditions in the interior of the experimental charge during an experiment.

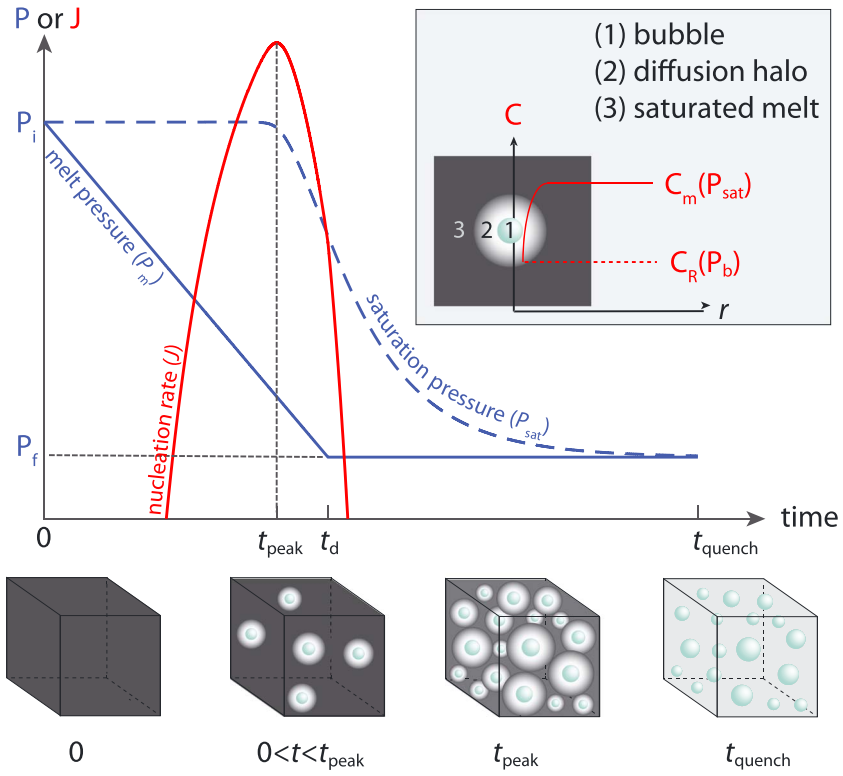

Figure 2. Schematic representation of bubble nucleation and growth for an experiment wherein nucleation peaks and ceases before the sample is quenched. Decompression starts at $t = 0$, when the melt is saturated with water and contains no bubbles. As pressure decreases the melt becomes supersaturated in water, bubbles nucleate, and water diffuses into bubbles. The inset illustrates that diffusion creates a halo of melt in the periphery of each bubble (labeled "1") wherein water concentration is less than the initial concentration (labeled "2"), which still exists outside of the halo (labeled "3"). At $t = t_{peak}$ diffusion has begun to reduce the initial water concentration throughout the entire melt. As a consequence, supersaturation pressure decreases and nucleation rate drops rapidly. At t_d decompression ceases and at t_{quench} the sample is quenched. It should be noted that the numerical model calculates the average water concentration, C_m, rather than the spatially varying concentration as schematically illustrated here.

Initial conditions of dependent variables at $t = 0$ are denoted by a subscript "i" throughout the text. All initial conditions are zero except for $C_{m,i}$ and $P_{m,i}$, which are based on experimental conditions (Table 3). $C_{m,i}$ is determined from the solubility model of Liu et al. (2005) at $P_{m,i}$. As P_m decreases the melt becomes supersaturated in H_2O and J increases (Figure 2). At the same time bubbles that have already nucleated will grow because the pressure within bubbles, P_b, is greater than P_m. Because of bubble growth P_b decreases and the concentration of water at the bubble-melt interface, which is assumed to be the solubility of water at pressure P_b, also decreases. This results in a concentration gradient between dissolved water at the bubble-melt interface (C_R) and the average concentration of water dissolved within the melt (C_m). As a consequence water will diffuse toward and into existing bubbles, and C_m will not only decrease by nucleation but also because water exsolves from the melt by diffusion. This decrease in C_m provides a negative feedback on nucleation rate by reducing the degree of supersaturation, $P_{sat} - P_m$. The model therefore simulates the balance between supersaturation-driven nucleation and diffusion-driven exsolution.

5.2. The Method of Moments

The number of bubbles in most experiments, and also in real volcanic systems, is too numerous to calculate the growth of individual bubbles from the time of nucleation. Instead, the process is simulated using the standard method of moments, which accounts for the evolution of population balance equations (Randolph & Larson, 1988; Toramaru, 2001). It was first used for bubble nucleation in magmas by Toramaru (1989, 1995). Assuming spatial averages, the kth order moment is defined as

$$M_k(t) = \int_{R_c}^{\infty} R^k F(R,t)\,\mathrm{d}R. \tag{13}$$

Here $F(R,t)$ is the length-based number density function, which is the number of bubbles per unit volume of melt at time $0 \leq t \leq t_{\text{quench}}$ and within the interval of radii ranging from R to $R + \mathrm{d}R$. Each moment of the bubble population is related to a measurable characteristic of the modeled system as defined below.

The zeroth moment is defined as

$$M_0(t) = \int_{R_c}^{\infty} F(R,t)\,\mathrm{d}R. \tag{14}$$

It is the bubble number density at time t, defined as the sum of all bubbles per volume of melt. The change in bubble number density with respect to time is the derivative of the zeroth moment with respect to time. In the absence of bubble coalescence and shrinkage it is equal to the nucleation rate

$$\frac{\mathrm{d}M_0}{\mathrm{d}t} = J, \tag{15}$$

where J is given by equation (4). Integration of equation (15) from the onset of decompression until quenching of the sample results in the predicted bubble number density, $N_{\text{m}}^{*} = M_0(t_{\text{quench}})$.

The first moment is defined as

$$M_1(t) = \int_{R_c}^{\infty} F(R,t)\,R\,\mathrm{d}R, \tag{16}$$

which is an indicative of mean bubble radius, $\bar{R} = M_1/M_0$. The motions for the first moment are given by

$$\frac{\mathrm{d}M_1}{\mathrm{d}t} = \frac{\mathrm{d}\bar{R}}{\mathrm{d}t}M_0 + \frac{\mathrm{d}M_0}{\mathrm{d}t}R_c. \tag{17}$$

The first term in the right-hand side is due to growth of existing bubbles, and the second term represents the nucleation of new bubbles, where R_{c} is the critical radius of a nucleating bubble as given by equation (7). The latter is often small compared to the first term and is neglected in the equations for motion of moments in Randolph and Larson (1988) and Toramaru (1995). However, we found it important at the early stages of nucleation, when $\bar{R} \sim R_{\text{c}}$, and consider it in our numerical computations of the first moment, and similar for the second and third moments.

The rate of bubble growth, $\mathrm{d}\bar{R}/\mathrm{d}t$, in equation (17) is calculated using the Rayleigh-Plesset equation (Plesset & Prosperetti, 1977) given as

$$P_{\text{b}} - P_{\text{m}} = \frac{2\gamma}{\bar{R}} + 4\eta\frac{1}{\bar{R}}\frac{\mathrm{d}\bar{R}}{\mathrm{d}t}, \tag{18}$$

if inertial terms are neglected, which is justified because they are sufficiently small compared to viscous forces under the conditions of our experiments (e.g., Prousevitch et al., 1993; Toramaru, 1995). Here η is the melt viscosity, calculated from the viscosity model of Hui and Zhang (2007) at C_{R} and T. Bubble growth occurs if the pressure difference of the fluid inside the bubble, P_{b}, and the surrounding melt, P_{m}, exceeds the Laplace pressure, $2\gamma/\bar{R}$. The value of P_{b} is calculated from the equation of state of Holloway (1977), at volume $4\pi\bar{R}^3/3$ and mass m_{g}/M_0, where m_{g} is the total mass of water in the fluid phase per unit volume of melt and given by equation (26).

The second moment is defined as

$$M_2(t) = \int_{R_c}^{\infty} R^2 F(R,t)\,\mathrm{d}R. \tag{19}$$

It corresponds to total surface area of bubbles (πM_2) per volume of melt. The motion of the second moment is defined as

$$\frac{\mathrm{d}M_2}{\mathrm{d}t} = 2\frac{\mathrm{d}\bar{R}}{\mathrm{d}t}M_1 + \frac{\mathrm{d}M_0}{\mathrm{d}t}R_c^2. \tag{20}$$

Finally, the third moment, defined as

$$M_3(t) = \int_{R_c}^{\infty} R^3 F(R,t)\,\mathrm{d}R, \tag{21}$$

is related to the volume fraction of bubbles, ϕ, as

$$\phi = \frac{(4/3)\pi M_3}{1 + (4/3)\pi M_3}. \tag{22}$$

The motion of the third moment is given by

$$\frac{\mathrm{d}M_3}{\mathrm{d}t} = 3\frac{\mathrm{d}\bar{R}}{\mathrm{d}t}M_2 + \frac{\mathrm{d}M_0}{\mathrm{d}t}R_c^3. \tag{23}$$

5.3. Average Water Concentration and Pressure

The concentration of water dissolved in the melt decreases as a consequence of water molecules clustering to form bubble nuclei and as a consequence of water molecules diffusing into existing bubbles. The latter is estimated from the conservation of mass:

$$\frac{\mathrm{d}m_\mathrm{b}}{\mathrm{d}t} = 4\pi\bar{R}^2\rho_\mathrm{m}q. \tag{24}$$

Here $\rho_\mathrm{m} = 2324$ kg/m^3 is the melt density calculated from Lange (1994) for the melt composition and temperature in our experiments. Changes in ρ_m, due to changes in the concentration of dissolved water and pressure during the experiments, are sufficiently small for the purposes of this model and are therefore neglected. The q is the mass flux of water diffusing into bubbles, calculated using the mean field approximation (Toramaru, 1995):

$$q = D\left(\frac{C_\mathrm{m} - C_\mathrm{R}}{\bar{R}}\right). \tag{25}$$

Here C_R is calculated from the solubility of Liu et al. (2005) at pressure P_b.

The rate of change in the total mass of the fluid phase, m_g, comprises the sixth differential equation of our model. It is given by

$$\frac{\mathrm{d}m_\mathrm{g}}{\mathrm{d}t} = M_0\frac{\mathrm{d}m_\mathrm{b}}{\mathrm{d}t} + \frac{\mathrm{d}M_0}{\mathrm{d}t}m_c. \tag{26}$$

The first term in the right-hand side of equation (26) is the diffusion of water into bubbles, given by equation (24). The second term is the addition of water to the fluid phase due to the nucleation of new bubbles. The variable m_c is the mass of a bubble nucleus, calculated using the equation of state at pressure P_nuc and volume $4\pi R_\mathrm{c}^3/3$. The average concentration of dissolved water in the melt is therefore given by

$$C_\mathrm{m} = C_\mathrm{m,i} - m_\mathrm{g}/\rho_\mathrm{m}. \tag{27}$$

The rate of change in melt pressure, P_m, constitutes the last equation and is given by

$$\begin{aligned} &\frac{\mathrm{d}P_\mathrm{m}}{\mathrm{d}t} = -\frac{P_\mathrm{i} - P_\mathrm{f}}{t_\mathrm{d}}, \quad \text{if} \quad 0 < t < t_\mathrm{d}, \\ &\text{and} \\ &\frac{\mathrm{d}P_\mathrm{m}}{\mathrm{d}t} = 0, \qquad\quad \text{if} \quad t_\mathrm{d}, \leqslant t \leqslant t_\mathrm{quench}. \end{aligned} \tag{28}$$

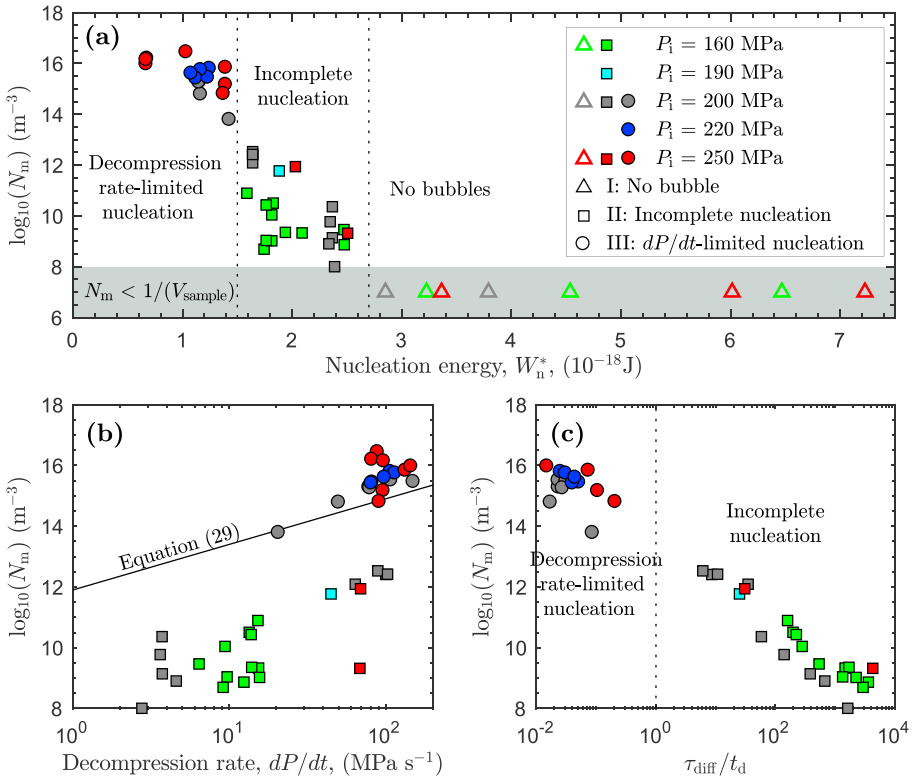

Figure 3. (a) Bubble number density, N_m, as a function of the empirical nucleation energy, W_n^*. (b) N_m as a function of decompression rate, dP/dt. Equation (29) for P_{sat} = 250 MPa and T = 850 °C (black line). (c) Ratio of diffusion timescale to decompression timescale, as a function of N_m. For $\tau_{diff}/t_d \gg 1$ nucleation is incomplete and independent of decompression rate, whereas for $\tau_{diff}/t_d \ll 1$ nucleation is controlled by decompression rate.

5.4. Summary of Governing Equations and Initial Conditions

The numerical model comprises six coupled ordinary differential equations: (15), (17), (20), (23), (26), and (28). They are integrated using the `ode15s` function of MATLAB® to obtain a predicted bubble number density, N_m^*. Initial conditions at $t = 0$ are as follows:

$$M_{0,1,2,3} = 0, m_g = 0, \text{and } P_m = P_i.$$

All parameters in the governing system of equations are either specified or calculated from existing formulations: Lange (1994) for melt density; Liu et al. (2005) for water solubility in rhyolite; Hui and Zhang (2007) for melt viscosity; Zhang and Behrens (2000) for water diffusivity given that their experimental conditions match ours; Holloway (1977) for fugacity of water, with modification of Flowers (1979) and Ochs and Lange (1999) for molecular volume of water; and Holloway (1977) for the equation of state of water.

6. Experimental Results

Bubble number density of the experiments ranges from no bubbles to over 10^{16} bubbles per 1 m^3 of melt (Figure 3). For each experiment N_m depends to various degrees on the nucleation energy, decompression rate, and duration of the experiment. The nucleation energy, W_n, corresponds to the energy barrier for the formation of a new interface between the fluid comprising a bubble nucleus and the surrounding melt. We obtain an estimate of the minimum nucleation energy for each experiment that is solely based on measurable parameters. It is denoted as W_n^* and based on equation (10), albeit at measured values $P_{sat} = P_i$, $P_m = P_f$, and surface tension calculated from equation (1) at initial water saturation. On the basis of N_m and W_n^* the experiments can be divided into three groups.

6.1. No Bubbles

These are experiments during which no bubbles nucleated. They correspond to conditions where the nucleation energy never reached sufficiently small values for bubbles to nucleate over the course of the

experiment. The experimental sample volume is on average approximately 10 mm^3, and samples with no bubbles imply $N_m < 10^8$ m^{-3}, corresponding to the shaded area in Figure 3a.

The transition from no bubbles to bubbles occurs at $W_n^* \approx 2.3 \times 10^{-18}$ J. In the absence of established experimental constraints on the nucleation time lag or the induction time (Schmelzer et al., 2017) we neglect both. Under this assumption bubbles nucleate in an experimental sample when $(J_{max}V)^{-1}$ is less than the time over which the sample was held at its final pressure. Here J_{max} is the maximum nucleation rate at P_f, and V is the sample volume.

6.2. Incomplete Nucleation

Figure 3b shows that experiments during which $<10^{13}$-m^{-3} bubbles nucleated fall far from the trend predicted by the bubble number density decompression rate meter of Toramaru (2006). A dependence of N_m on decompression rate is expected if bubble number densities are large and the distance between bubbles is small so that diffusive volatile exsolution affects supersatuartion at similar rates as decompression (Gonnermann & Gardner, 2013; Hamada et al., 2010; Mourtada-Bonnefoi & Laporte, 2004; Toramaru, 1989, 1995). This dependence was quantified by Toramaru (2006) as the "bubble number density decompression rate meter" and is given by

$$N_m^* \sim a\, D^{-3/2}\, \gamma_B^{-3}\, P_{sat}^{1/2}\, T^{3/4} \left(\frac{dP}{dt}\right)^{3/2}, \tag{29}$$

where $a = 3.16 \times 10^{-23}$ is a constant. Experiments with bubble number densities of up to 10^{13} m^{-3}, corresponding to 1.3×10^{-18} J $\lessapprox W_n \lessapprox 2.3 \times 10^{-18}$ J, cannot be predicted by equation (29) because N_m remained too low for diffusion to affect saturation. As a consequence nucleation proceeded at its maximum possible rate until the sample was quenched, which is before nucleation had run its course. There was little or no dependence on decompression rate, which is the basis of equation (29). Allabar and Nowak (2018) also observed decompression-independent bubble number densities in decompression experiments, albeit in hydrated phonolitic melts. In contrast to our experiments with decompression-independent bubble number densities, for their experiments, the diffusion timescale at final bubble number densities is much smaller than the experimental time. Allabar and Nowak's (2018) experiments therefore do not fall into the incomplete nucleation regime; instead, they interpret their results as indicative of spinodal decomposition.

The relative importance of diffusion during decompression can be quantified through the ratio of the diffusion timescale, τ_{diff}, to the decompression time, t_d, where we define τ_{diff} as

$$\tau_{diff} \equiv \frac{l^2}{D}. \tag{30}$$

Here l is characteristic diffusion length, calculated from N_m and ϕ as (Mourtada-Bonnefoi & Laporte, 2002; Navon & Lyakhovsky, 1998)

$$l = \frac{1-\phi^{1/3}}{(1-\phi)^{1/3}} \left(\frac{4\pi}{3} N_m\right)^{-1/3}, \tag{31}$$

and D is calculated from Zhang and Behrens (2000) at the initial water saturation. For experiments with small ϕ we approximate l as $(4\pi/3\,N_m)^{-1/3}$. We note that our ratio τ_{diff}/t_d is different from the parameter α_3 defined by Toramaru (1995), which is based on a diffusion length proportional to the critical bubble radius. For experiments where $\tau_{diff}/t_d \gg 1$ water diffusion into nucleated bubbles will be too slow to significantly affect saturation within the bulk of the sample. In our experiments this is the case for samples with $N_m \lesssim 10^{13}$ m^{-3} (Figure 3c).

6.3. Decompression Rate Limited Nucleation

Experiments during which $>10^{13}$ m^{-3} bubbles nucleated fall on or near the trend predicted by the bubble number density decompression rate meter of Toramaru (2006). N_m depends on decompression rate if bubble number densities reach sufficiently high values for volatile diffusion to affect saturation. In this case the maximum supersaturation depends on the relative balance between decompression and diffusion. As a consequence there is an expected dependence of N_m on decompression rate (Figure 3b). Although bubble number densities predicted on the basis of equation (30) approximate the observed values for samples with $\tau_{diff}/t_d \ll 1$ far better than for samples with $\tau_{diff}/t_d \gg 1$, further room for improvements exist.

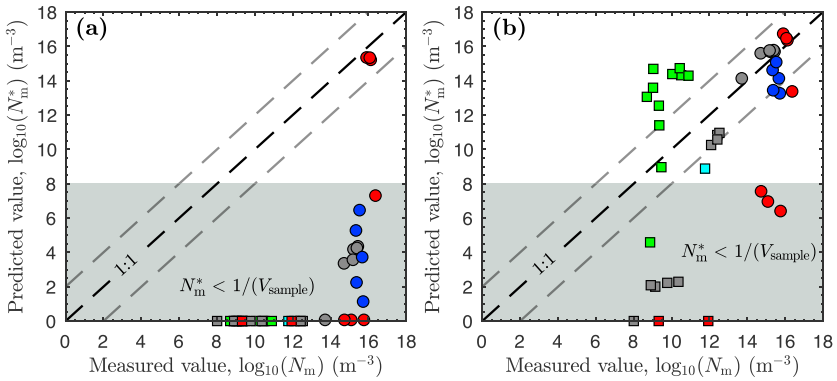

Figure 4. Comparison of observed bubble number density, N_m, with those predicted by the model, N^*_m, using surface tension based on (a) equation (1) and (b) equation (2). Symbols are the same as in Figure 3.

7. Numerical Modeling of Bubble Nucleation and Prediction of N_m

Our ultimate goal is to improve the reliability by which we can simulate bubble nucleation during volcanic eruptions. A critical first step in this direction is the ability to predict bubble nucleation during experiments where pressure and water saturation are known. To this end we performed numerical simulations of bubble nucleation within our experiments. The prediction of an experimental sample's bubble number density is dependent on the value of $W_n(t)$, given by equation (10). It depends on the evolving pressures $P_n(t)$ and $P_m(t)$, and on $\gamma(t)$. The value of $P_m(t)$ is experimentally controlled and known for each experiment. $P_n(t)$ can be calculated from equation (8). In contrast $\gamma(t)$ can neither be measured nor calculated directly. It is thought to be different from the macroscopically measurable surface tension because of the dependence on nucleus size (Tolman, 1949), which is thus far unconstrained for silicate melts.

We therefore have to constrain γ, together with its dependence on water saturation and nucleus size. We do so through repeated numerical simulation of bubble nucleation, where each simulation suite uses a different functional parameterization of $\gamma = f(\delta, \alpha, \gamma_B)$ for all experiments. The empirical parameters that are varied from one simulation suite to another are δ, the Tolman length, and α. The latter accounts for the difference in macroscopic surface tension between our rhyolitic samples and the γ_B function for haplogranitic melt. Allowing for such potential discrepancies in macroscopic surface tension may be justified because of compositional differences. Furthermore, potential measurement error or bias in the measurements upon which γ_B is based cannot be ruled out, given that these experiments have never been reproduced.

We thus seek constant values of δ and α that yield a best fit between the measured and simulated values of bubble number density for all experiments combined. The necessity of this approach is demonstrated by the fact that simulations, which use the existing formulations of surface tension (equations (1) and (2)), cannot adequately predict bubble number density to within orders of magnitude for almost all experiments (Figure 4). The need for a functional form that allows simultaneously for the nonconstancy of γ and a deviation from γ_B is illustrated by the results of simulations that provide an exact match to the measured bubble number densities for each experiment while assuming a constant value of γ for each experiment separately. Figure 5, which shows the results of these simulations, indicates that a simple dependence of surface tension on water saturation and temperature is unlikely. Moreover, it shows that surface tension of a bubble nucleus is lower than the macroscopically measured values (γ_B), indicating that nucleation energy must be smaller than the estimated empirical values $W^*_n(\gamma_B)$ shown in Figure 3 and in Table 3.

7.1. The Functional Form of Surface Tension During Bubble Nucleation

In the subsequent paragraphs we discuss the rationale for the functional form of $\gamma = f(\delta, \alpha, \gamma_B)$, and we describe how estimates for the empirical constants δ and α were obtained. To allow for a nonconstant surface tension, we use the correction proposed by Tolman (1949), which is given by equation (3). The Tolman correction postulates that surface tension of small droplets and bubbles deviates from the surface tension of a planar interface. The Tolman correction is based on the ratio of the Tolamn length, δ, and the radius of surface of tension, R_s. The surface of tension is the Gibbs dividing surface, and its radius depends on the

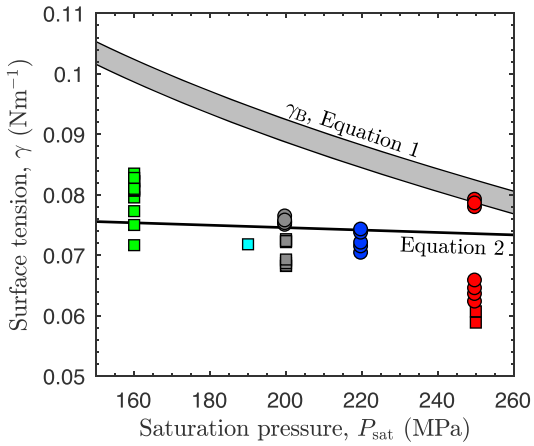

Figure 5. The constant value of surface tension, γ, for each individual experiment that results in a perfect match to the measured bubble number density. The shaded area shows γ_B from equation (1) at 825–875 °C. The solid line represents the surface tension from equation (2) at 850 °C. Symbols are the same as in Figure 3.

capillary pressure, given by equation (7). The Tolman length is given by

$$\delta \equiv \lim_{P_s \to \infty} (R_e - R_s), \tag{32}$$

where R_e is the radius of the equimolar dividing surface. The equimolar dividing surface is based on the molar concentration of H_2O, denoted as ε. Across the diffuse interface between bubble nucleus and melt the molar concentration of H_2O changes gradually, as illustrated by the red solid line in Figure 6. The hypothetical equimolar dividing surface corresponds to a sharp interface across which the molar concentration changes sharply, as illustrated by the red dashed line in Figure 6. The radial position of this hypothetical equimolar dividing surface is defined by the value of r at which the function

$$\Gamma(r) = \int_{-\infty}^{r} \left(\varepsilon^{\text{fluid}} - \varepsilon(r)\right) \mathrm{d}r + \int_{r}^{+\infty} \left(\varepsilon^{\text{melt}} - \varepsilon(r)\right) \mathrm{d}r \tag{33}$$

vanishes; that is, $\Gamma(R_e) = \Gamma(r) = 0$.

The Tolman correction requires that the surface tension of a planar interface, denoted as γ_∞, is known. This is, however, not the case for rhyolitic melt. The most relevant surface tension measurements are those by Bagdassarov et al. (2000) for haplogranitic melt, which may differ from rhyolitic melt. To account for potential discrepancies between γ_∞ of the rhyolitic melt used in our experiments and the data upon which γ_B is based, we introduce the correction factor, α, defined as

$$\gamma_\infty = (1 + \alpha)\gamma_B. \tag{34}$$

The linear form of this correction was assumed in order to retain the original exponential form of γ_B and, furthermore, to keep the number of unknown variables to a minimum. The resultant equation for the Tolman-corrected surface tension of bubble nuclei in rhyolitic melt becomes

$$\gamma = \frac{1 + \alpha}{1 + 2\delta/R_s} \quad \gamma_B. \tag{35}$$

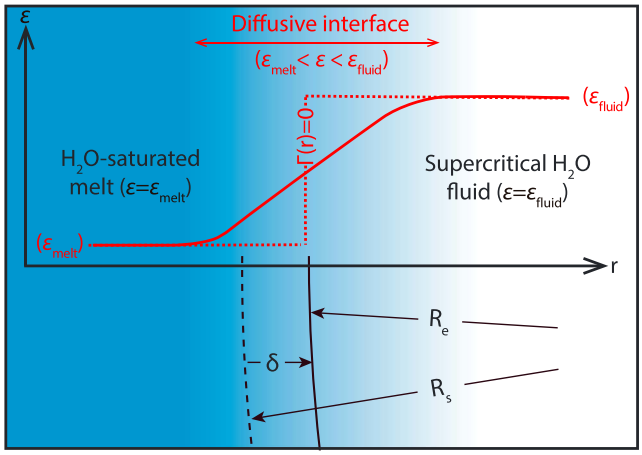

Figure 6. A schematic of the diffusive interface between H_2O fluid and melt where quantities such as the molar concentration of H_2O changes gradually. Also shown are the equimolar dividing surface of radius, R_e, the radius of curvature for surface of tension, R_s, and the hypothetical molar concentration of H_2O. Tolman (1949) places the origin of the radial coordinate within the liquid (melt) phase, in which case R_e <0 and R_s < 0 for bubbles (Schmelzer & Baidakov, 2016).

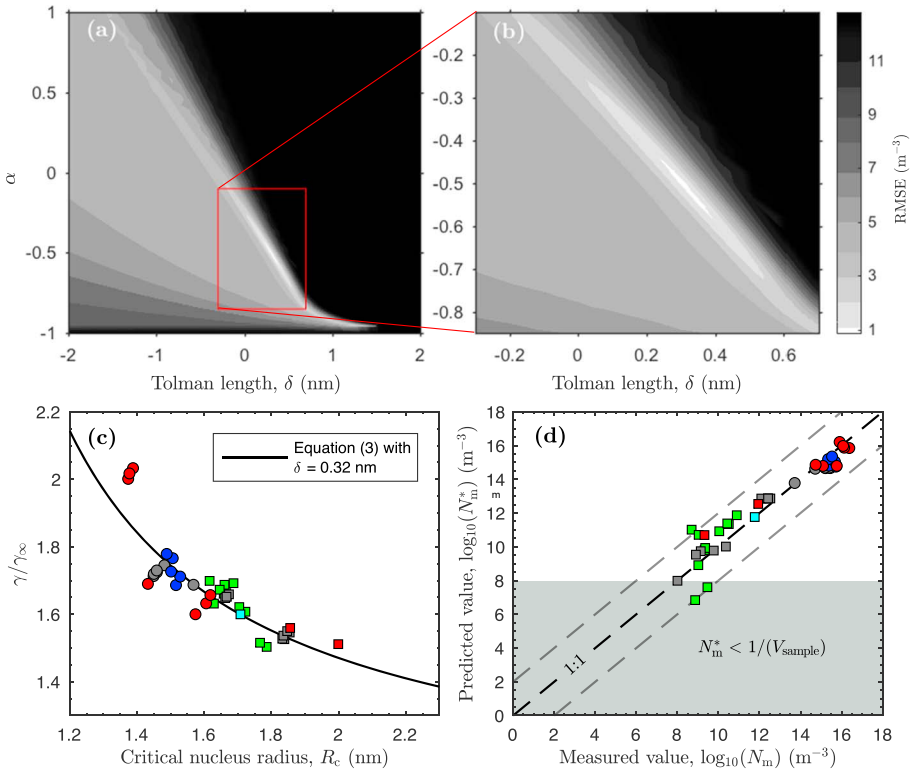

Figure 7. (a, b) Root-mean-square error as a function of the Tolman length, δ, and parameter α. The minimum root-mean-square error is 0.86 m^{-3}. The red box in (a) indicates the range in α and δ shown in (b). (c) Ratio of γ to γ_∞ for each experiment as a function of critical nucleus radius, R_c. The curve is given by equation (3) with $\delta = 0.32$ nm. (d) Comparison of observed and predicted bubble number densities. Symbols are the same as in Figure 3.

7.2. Estimation of Surface Tension and Discussion of Results

7.2.1. Results of the Parameter Estimation

The values for the empirical constants α and δ were estimated by numerical modeling of bubble nucleation in the experiments. The α and δ were varied systematically within empirical bounds. For each combination of α and δ nucleation in each experiment was simulated and the root-mean-square error (RMSE) between the logarithm of model predictions of bubble number density and measured values was calculated. We define the root-mean-square error as

$$\mathrm{RMSE} = \sqrt{\sum_{j=1}^{k} \frac{1}{k} \left(\log_{10}(N_{\mathrm{m},j}) - \log_{10}(N^*_{\mathrm{m},j}) \right)^2}, \tag{36}$$

where j denotes the jth experiment and k=41. The objective of the grid search is to find the value combination of α and δ that minimizes the RMSE.

Figures 7a and 7b show that a search over -2 nm $\leq \delta \leq 2$ nm and $-1 \leq \alpha \leq 1$ yields a global minimum in RMSE of 0.86 at $\delta = 0.32$ nm and $\alpha = -0.51$. The corresponding functional relation is shown in Figure 7c. The comparison between predicted and actual bubble number densities is shown in Figure 7d. Simulations for experiments that produced no bubbles, which are not shown in Figure 7d, resulted in $N^*_{\mathrm{m}} \ll 10^8$ m^{-3} and corresponds to zero bubbles within the experimental charge. The value of $\alpha = -0.51$ indicates that our estimates for the macroscopic surface tension of water bubbles in rhyolitic melt, γ_∞, are lower than the the surface tension data of Bagdassarov et al. (2000) for haplogranitic melt, represented by the function γ_B of equation (1) at equivalent temperatures. We have no explanation for this difference, but note that most experimental estimates of surface tension shown in Figure 1 fall below the data trend of Bagdassarov et al. (2000). In our opinion it would be desirable to obtain macroscopic surface tension measurements in rhyolitic melt, using similar or different techniques as Bagdassarov et al. (2000). In the absence of such data, the most conservative assumption is that γ_∞ follows a water saturation dependence similar to that found

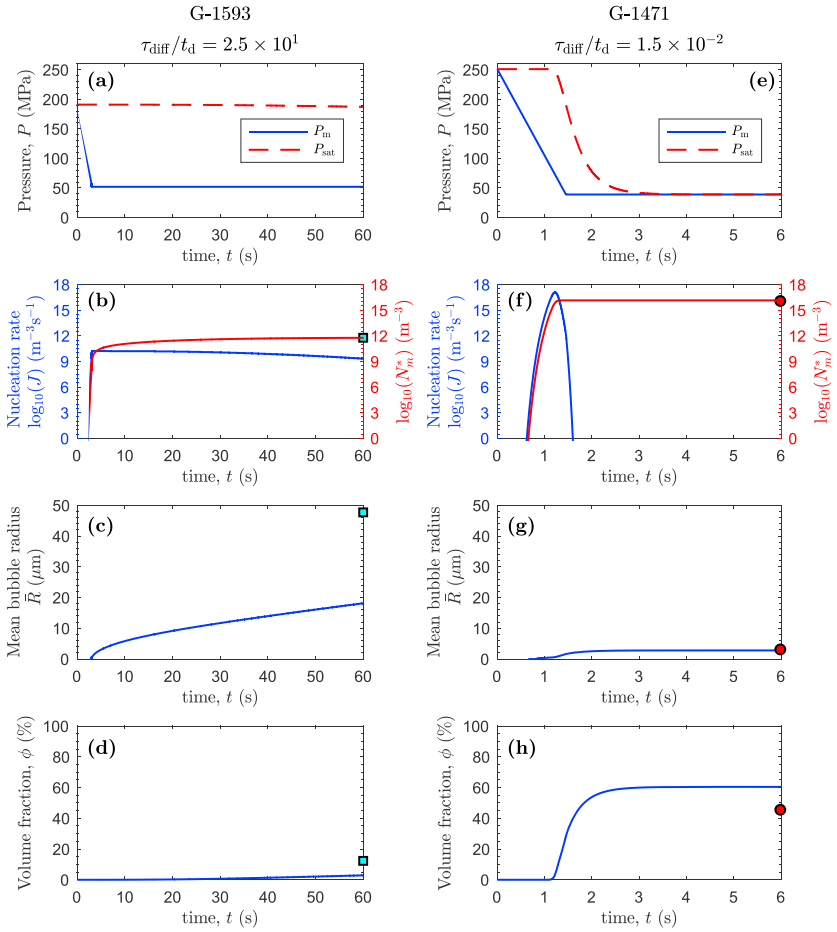

Figure 8. Calculated temporal progression of two experiments: G-1593 with $\tau_{diff}/t_d \gg 1$ (left column) and G-1471 with $\tau_{diff}/t_d \ll 1$ (right column). (a) and (e) show melt pressure, P_m, a prescribed parameter and saturation pressure, P_{sat}, which is the calculated pressure at which the melt would be saturated at the concentration of water that is dissolved. (b) and (f) show nucleation rate, J, and bubble number density, N_m^*. Symbols at $t = t_{quench}$ represent the actual bubble number density measured in the sample. (c) and (g) show the mean bubble radius, $\bar{R}$, whereas (d) and (h) show the volume fraction of bubbles, ϕ.

by Bagdassarov et al. (2000). Under this assumption, the value of $\delta = 0.32$ nm confirms a dependence of surface tension on the size of bubble nucleus, with increasing surface tension as nucleus size decreases. The improved fit between predicted and measured bubble number densities, or equivalently nucleation rates, that is achieved through these corrections is consistent with results on nucleation kinetics in general, where corrections to the classical theory yield vast improvements in predicted nucleation rates (Joswiak et al., 2013; Lubetkin, 2003)

7.2.2. Improvement of Predictive Capabilities

For the majority of experiments N_m is predicted to within an order of magnitude. There are, however, a few cases where the difference between N_m^* and N_m is about 2 orders of magnitude. Altogether, our new formulation for γ enables the prediction of homogeneous bubble nucleation in rhyolitic melts with significantly improved accuracy in comparison to previous formulations (Figure 4). The improvements are particularly notable for experiments with $N_m \lesssim 10^{13}$ m^{-3}, which are experiments where $\tau_{diff}/t_d \gg 1$ (Table 3). Here, the rate of bubble nucleation is to first order controlled by the supersaturation at the end of the decompression, $(P_i - P_f)$ and, more importantly, nucleation rate is very sensitive to surface tension and largely unaffected by diffusion or decompression rate. In contrast, experiments with $\tau_{diff}/t_d \ll 1$ are controlled by the interplay between diffusion and decompression and are relatively insensitive to surface tension. Although the fit between observations and model predictions could potentially be improved with additional degrees of freedom in the functional form of γ, there is no theoretical basis to justify this. In our opinion a more fruitful next step would be to test of our γ function against an independent suite of experiments.

7.2.3. The Tolman Length

Despite significant efforts to constrain δ, its magnitude and sign for one-component systems remain controversial (e.g., Baidakov et al., 2000; Joswiak et al., 2013; Lei et al., 2005; Malijevský & Jackson, 2012). For our multicomponent rhyolitic melt, the molar concentration H_2O in the supercritical fluid phase is higher than in the liquid phase, in contrast to one-component vapor-liquid systems. Perhaps, this explains why our analysis results in a positive Tolman length, which implies that the surface of tension is located at a larger distance from the bubble than the equimolar dividing surface (Figure 6).

7.2.4. Decompression Rate Dependence and "Incomplete" Nucleation

Figure 8 shows the modeled temporal evolution of two experiments. It illustrates the difference between experiments with $\tau_{diff}/t_d \gg 1$ (left column, G-1593) and those with $\tau_{diff}/t_d \ll 1$ (right column, G-1471). Both experiments underwent decompression at an approximately constant rate during the time interval $0 < t \leq t_d$. Following decompression the samples were held at P_f until $t = t_{quench}$, at which time the sample was quenched.

During experiment G-1593, for which $\tau_{diff}/t_d \gg 1$, water diffusion into existing bubbles is predicted to be too slow to significantly affect the average water saturation in the melt (Figure 8a). At t_d the melt is still fully saturated and remains so until t_{quench}. The nucleation rate reaches a maximum at t_d, when supersaturation reaches its maximum value, and it remains approximately constant until t_{quench}. Consequently, N_m^* increases linearly between t_d and t_{quench} (Figure 8b). The average bubble radius and volume fraction of bubbles increase at a high rate shortly after bubble nucleation and, due to diffusion, grow gradually until the sample is quenched (Figures 8c and 8d). We attribute the underprediction of $\bar{R}$ and ϕ to the approximation of water diffusion by the mean field approximation (equation (25)). Allowing for more diffusion by ad hoc increasing water diffusivity, while keeping all else the same, improves the match in $\bar{R}$ and ϕ between models and experiments but does not significantly affect N_m^*. We therefore conclude that our model results for surface tension are not significantly affected by the mean field approximation. That being said, future improvements of the model could include an improved approximation for the diffusive flux (Forestier-Coste et al., 2012). Overall, the volume fraction of bubbles, ϕ, remains low throughout the experiment, because most of the water remains dissolved in the melt (Figure 8d), because the experiment was terminated and the sample was quenched while bubbles were still nucleating. In other words, nucleation was incomplete.

During experiment G-1471, for which $\tau_{diff}/t_d \ll 1$, diffusion is predicted to reduce the saturation pressure, P_{sat}, before the sample reaches P_f (Figure 8e). Consequently, the nucleation rate peaks when P_{sat} begins to decrease (Figure 8f). The rapid diffusion of water into bubbles is a consequence of the high nucleation rates and resulting large bubble number densities. As bubble number density increases the average distance between adjacent bubbles decreases. This equates to a shorter diffusion length and a corresponding reduction in τ_{diff}. Once diffusion starts to affect water saturation the nucleation rate drops rapidly. As a consequence, nucleation peaks at high rates within a narrow time interval and results in large values of N_m^* (Figure 8f).

The average bubble radius grows rapidly but reaches a steady value shortly after nucleation, because water concentration decreases to its equilibrium value and diffusion stops. The volume fraction of bubbles reaches a relatively large value, because most of the dissolved water has exsolved (Figure 8h). For experiments with $\tau_{diff}/t_d \ll 1$, a small increase (decrease) in γ will shift the nucleation peak to later (earlier) times. However, the change in γ will be compensated by a change in supersaturation pressure and nucleation rate will peak at approximately the same value, albeit at a slightly different time. Therefore, N_m^* is essentially insensitive to γ for experiments with $\tau_{diff}/t_d \ll 1$. Instead, these experiments are sensitive to decompression rate, because of the competing effects of diffusion and decompression: Nucleation rate increases if decompression rate is higher than the reduction in supersaturation by diffusive water exsolution.

8. Conclusion

We performed bubble nucleation experiments in water saturated rhyolitic melt. Together with prior experiments, they constitute a coherent suite of experiments that span a wide range of saturation conditions and decompression rates. We used the method of moments to model bubble nucleation and growth in each experiment. We provide a function for surface tension that is capable of predicting bubble number density to within approximately 1 order of magnitude for most of our experiments. Our surface tension function is based on two empirical constants, one of which is the Tolman length. We find two nucleation regimes in our

experiments. They can be distinguished on the basis of the ratio of the diffusion timescale to the decompression timescale, denoted as τ_{diff}/t_d. At high (small) bubble number densities the average distance between bubbles and the diffusion timescale are low (large).

For $\tau_{diff}/t_d \ll 1$ nucleation is controlled by the balance between decompression and diffusion. This regime is associated with bubble number densities of $>10^{15}$ m^{-3}, high decompression rates, large supersaturation pressures, high nucleation rates, and a peak in nucleation before the final pressure is reached. Nucleation is sensitive to decompression rate but relatively insensitive to surface tension. We surmise that nucleation during high intensity explosive eruptions fall in this regime. Our results implicitly confirm the requirement for decompression rates of approximately 100 MPa/s for bubble number densities of $>10^{15}$ m^{-3}, assuming nucleation is homogeneous and, perhaps, consistent with a peak in nucleation near the level of fragmentation (Massol & Koyaguchi, 2005; Toramaru, 2014).

For $\tau_{diff}/t_d \gg 1$ bubble number densities are $<10^{13}$ m^{-3} and the nucleation energy remains at values of approximately higher than 1.5×10^{-18} J. Nucleation is relatively unaffected by diffusion and therefore insensitive to decompression rate. Model simulations predict that nucleation proceeds at near-constant rates until bubble number densities reach a sufficient value to reduce saturation pressure, which did not occur in any of our experiments because the samples were quenched before then. Thus, nucleation was incomplete. These results imply that, during eruptions with relatively low decompression rates, nucleation may occur over durations of minutes or longer while supersaturation remains low. The resultant distribution of bubbles would span a wide range in sizes. A subsequent sharp increase in nucleation rate may occur, if the decompression rate accelerates. Nucleation rate would reach a maximum once diffusion begins to affect supersaturation. The resultant bubble size distribution would be skewed toward small sizes (e.g., Adams et al., 2006; Klug & Cashman, 1994; Toramaru, 1990).

Acknowledgments
We thank L. Gurioli and one anonymous reviewer for their valuable suggestions and comments. This material is based upon work supported by the National Science Foundation grants EAR-1348072 and EAR-1348050. The computational work was supported by Rice University Computing Infrastructure funded by Rice University and NSF under grants OCI-0959097 and CNS-1338099. The data used are listed in the references and tables.

References

Abraham, F. F. (1974). *Homogeneous nucleation theory: The pretransition theory of vapor condensation*. New York, NY: Academic Press.

Adams, N. K., Houghton, B. F., & Hildreth, W. (2006). Abrupt transitions during sustained explosive eruptions: Examples from the 1912 eruption of Novarupta, Alaska. *Bulletin of Volcanology*, *69*(2), 189–206. https://doi.org/10.1007/s00445-006-0067-4

Alfano, F., Bonadonna, C., & Gurioli, L. (2012). Insights into eruption dynamics from textural analysis: The case of the May, 2008, Chaitén eruption. *Bulletin of Volcanology*, *74*(9), 2095–2108. https://doi.org/10.1007/s00445-012-0648-3

Allabar, A., & Nowak, M. (2018). Message in a bottle: Spontaneous phase separation of hydrous Vesuvius melt even at low decompression rates. *Earth and Planetary Science Letters*, *501*, 192–201. https://doi.org/10.1016/j.epsl.2018.08.047

Bagdassarov, N., Dorfman, A., & Dingwell, D. B. (2000). Effect of alkalis, phosphorus, and water on the surface tension of haplogranite melt. *American Mineralogist*, *85*(1), 33–40. https://doi.org/10.2138/am-2000-0105

Baidakov, V. G., Boltashev, G. S., & Schmelzer, J. W. (2000). Comparison of different approaches to the determination of the work of critical cluster formation. *Journal of Colloid and Interface Science*, *231*(2), 312–321. https://doi.org/10.1006/jcis.2000.7148

Carey, R., Houghton, B., & Thordarson, T. (2009). Abrupt shifts between wet and dry phases of the 1875 eruption of Askja Volcano: Microscopic evidence for macroscopic dynamics. *Journal of Volcanology and Geothermal Research*, *184*(3-4), 256–270. https://doi.org/10.1016/j.jvolgeores.2009.04.003

Cluzel, N., Laporte, D., Provost, A., & Kannewischer, I. (2008). Kinetics of heterogeneous bubble nucleation in rhyolitic melts: Implications for the number density of bubbles in volcanic conduits and for pumice textures. *Contributions to Mineralogy and Petrology*, *156*(6), 745–763. https://doi.org/10.1007/s00410-008-0313-1

Debenedetti, P. G. (1996). *Metastable liquids: Concepts and principles*. Princeton, NJ: Princeton University Press.

Epel'baum, M. (1973). Surface tension of felsic magmatic melts at high temperatures and pressure. *Geochemistry International*, *10*, 343–345.

Fiege, A., & Cichy, S. B. (2015). Experimental constraints on bubble formation and growth during magma ascent: A review. *American Mineralogist*, *100*(11-12), 2426–2442. https://doi.org/10.2138/am-2015-5296

Fisher, L. R., & Israelachvili, J. N. (1981). Experimental studies on the applicability of the kelvin equation to highly curved concave menisci. *Journal of Colloid and Interface Science*, *80*(2), 528–541. https://doi.org/10.1016/0021-9797(81)90212-5

Flowers, G. C. (1979). Correction of Holloway's (1977) adaptation of the modified Redlich-Kwong equation of state for calculation of the fugacities of molecular species in supercritical fluids of geologic interest. *Contributions to Mineralogy and Petrology*, *69*(3), 315–318. https://doi.org/10.1007/BF00372333

Forestier-Coste, L., Mancini, S., Burgisser, A., & James, F. (2012). Numerical resolution of a mono-disperse model of bubble growth in magmas. *Applied Mathematical Modelling*, *36*(12), 5936–5951. https://doi.org/10.1016/j.apm.2012.01.031

Gardner, J. E., Hajimirza, S., Webster, J. D., & Gonnermann, H. M. (2018). The impact of dissolved fluorine on bubble nucleation in hydrous rhyolite melts. *Geochimica et Cosmochimica Acta*, *226*, 174–181. https://doi.org/10.1016/j.gca.2018.02.013

Gardner, J. E., Hilton, M., & Carroll, M. R. (1999). Experimental constraints on degassing of magma: Isothermal bubble growth during continuous decompression from high pressure. *Earth and Planetary Science Letters*, *168*(1-2), 201–218. https://doi.org/10.1016/s0012-821x(99)00051-5

Gardner, J. E., & Ketcham, R. A. (2011). Bubble nucleation in rhyolite and dacite melts: Temperature dependence of surface tension. *Contributions to Mineralogy and Petrology*, *162*(5), 929–943. https://doi.org/10.1007/s00410-011-0632-5

Gardner, J. E., Ketcham, R. A., & Moore, G. (2013). Surface tension of hydrous silicate melts: Constraints on the impact of melt composition. *Journal of Volcanology and Geothermal Research*, *267*, 68–74. https://doi.org/10.1016/j.jvolgeores.2013.09.007

Giachetti, T., Druitt, T. H., Burgisser, A., Arbaret, L., & Galven, C. (2010). Bubble nucleation, growth and coalescence during the 1997 Vulcanian explosions of Soufriére Hills Volcano, Montserrat. *Journal of Volcanology and Geothermal Research*, *193*(3-4), 215–231. https://doi.org/10.1016/j.jvolgeores.2010.04.001

Giachetti, T., Gonnermann, H. M., Gardner, J. E., Burgisser, A., Hajimirza, S., Early, T. C., et al. (2019). Bubble coalescence and percolation threshold in expanding rhyolitic magma. *Geochemistry, Geophysics, Geosystems*, *20*. https://doi.org/10.1029/2018GC008006

Gibbs, J. W. (1961). The scientific papers of J. Willard Gibbs (PhD), LL.D. vol. 1: Thermodynamics, Dover, New York, NY.

Gondé, C., Martel, C., Pichavant, M., & Bureau, H. (2011). In situ bubble vesiculation in silicic magmas. *American Mineralogist*, *96*(1), 111–124. https://doi.org/10.2138/am.2011.3546

Gonnermann, H. M., & Gardner, J. E. (2013). Homogeneous bubble nucleation in rhyolitic melt: Experiments and nonclassical theory. *Geochemistry, Geophysics, Geosystems*, *14*, 4758–4773. https://doi.org/10.1002/ggge.20281

Gonnermann, H. M., & Manga, M. (2005). Nonequilibrium magma degassing: Results from modeling of the ca. 1340 A.D. eruption of Mono Craters, California. *Earth and Planetary Science Letters*, *238*(1-2), 1–16. https://doi.org/10.1016/j.epsl.2005.07.021

Gonnermann, H. M., & Manga, M. (2007). The fluid mechanics inside a volcano. *Annual Review of Fluid Mechanics*, *39*(1), 321–356. https://doi.org/10.1146/annurev.fluid.39.050905.110207

Gurioli, L., Houghton, B. F., Cashman, K. V., & Cioni, R. (2005). Complex changes in eruption dynamics during the 79 AD eruption of Vesuvius. *Bulletin of Volcanology*, *67*(2), 144–159. https://doi.org/10.1007/s00445-004-0368-4

Hamada, M., Laporte, D., Cluzel, N., Koga, K. T., & Kawamoto, T. (2010). Simulating bubble number density of rhyolitic pumices from Plinian eruptions: Constraints from fast decompression experiments. *Bulletin of Volcanology*, *72*(6), 735–746. https://doi.org/10.1007/s00445-010-0353-z

Hirth, J. P., Pound, G. M., & Pierre, G. R. S. (1970). Bubble nucleation. *Metallurgical Transactions*, *1*(4), 939–945. https://doi.org/10.1007/BF02811776

Holloway, J. R. (1977). *Fugacity and activity of molecular species in supercritical fluids, 161–181 pp.*Dordrecht, Netherlands: Springer Netherlands. https://doi.org/10.1007/978-94-010-1252-2_9

Houghton, B. F., Carey, R. J., Cashman, K. V., Wilson, C. J. N., Hobden, B. J., & Hammer, J. E. (2010). Diverse patterns of ascent, degassing, and eruption of rhyolite magma during the 1.8 ka Taupo eruption, New Zealand: Evidence from clast vesicularity. *Journal of Volcanology and Geothermal Research*, *195*(1), 31–47. https://doi.org/10.1016/j.jvolgeores.2010.06.002

Hui, H., & Zhang, Y. (2007). Toward a general viscosity equation for natural anhydrous and hydrous silicate melts. *Geochimica et Cosmochimica Acta*, *71*(2), 403–416. https://doi.org/10.1016/j.gca.2006.09.003

Hurwitz, S., & Navon, O. (1994). Bubble nucleation in rhyolitic melts: Experiments at high pressure, temperature, and water content. *Earth and Planetary Science Letters*, *122*(3-4), 267–280. https://doi.org/10.1016/0012-821x(94)90001-9

Johnson, M. C., Anderson, A. T., & Rutherford, M. J. (1994). Pre-eruptive volatile contents of magmas. *Reviews in Mineralogy and Geochemistry*, *30*(1), 281.

Joswiak, M. N., Duff, N., Doherty, M. F., & Peters, B. (2013). Size-dependent surface free energy and Tolman-corrected droplet nucleation of TIP 4p/2005 water. *The Journal of Physical Chemistry Letters*, *4*(24), 4267–4272. https://doi.org/10.1021/jz402226p

Khitarov, N. I., Lebedev, E. B., Dorfman, A. M., & Bagdasarov, N. S. (1979). Effects of temperature, pressure and volatiles on the surface tension of molten basaltic. *Geochemistry International*, *16*(5), 78–86.

Klug, C., & Cashman, K. V. (1994). Vesiculation of May 18, 1980, Mount St. Helens magma. *Geology*, *22*(5), 468–472. https://doi.org/10.1130/0091-7613(1994)022<0468:VOMMSH>2.3.CO;2

Klug, C., Cashman, K. V., & Bacon, C. R. (2002). Structure and physical characteristics of pumice from the climactic eruption of Mount Mazama (Crater Lake), Oregon. *Bulletin of Volcanology*, *64*(7), 486–501. https://doi.org/10.1007/s00445-002-0230-5

Lange, R. A. (1994). The effect of H_2O, CO_2 and F on the density and viscosity of silicate melts. *Reviews in Mineralogy and Geochemistry*, *30*(1), 331–369.

Lei, Y. A., Bykov, T., Yoo, S., & Zeng, X. C. (2005). The Tolman length: Is it positive or negative? *Journal of the American Chemical Society*, *127*(44), 15,346–15,347. https://doi.org/10.1021/ja054297i

Lensky, N. G., Navon, O., & Lyakhovsky, V. (2004). Bubble growth during decompression of magma: Experimental and theoretical investigation. *Journal of Volcanology and Geothermal Research*, *129*(1-3), 7–22. https://doi.org/10.1016/s0377-0273(03)00229-4

Liu, Y., Zhang, Y., & Behrens, H. (2005). Solubility of H_2O in rhyolitic melts at low pressures and a new empirical model for mixed H_2O– CO_2 solubility in rhyolitic melts. *Journal of Volcanology and Geothermal Research*, *143*(1-3), 219–235. https://doi.org/10.1016/j.jvolgeores.2004.09.019

Lubetkin, S. D. (2003). Why is it much easier to nucleate gas bubbles than theory predicts? *Langmuir*, *19*(7), 2575–2587. https://doi.org/10.1021/la0266381

Malijevský, A., & Jackson, G. (2012). A perspective on the interfacial properties of nanoscopic liquid drops. *Journal of Physics Condensed Matter*, *24*(464121). https://doi.org/10.1088/0953-8984/24/46/464121

Mangan, M., & Sisson, T. (2000). Delayed, disequilibrium degassing in rhyolite magma: Decompression experiments and implications for explosive volcanism. *Earth and Planetary Science Letters*, *183*(3-4), 441–455. https://doi.org/10.1016/s0012-821x(00)00299-5

Mangan, M., & Sisson, T. (2005). Evolution of melt-vapor surface tension in silicic volcanic systems: Experiments with hydrous melts. *Journal of Geophysical Research*, *110*, B01202. https://doi.org/10.1029/2004jb003215

Marziano, G. I., Schmidt, B. C., & Dolfi, D. (2007). Equilibrium and disequilibrium degassing of a phonolitic melt (Vesuvius AD 79 “white pumice”) simulated by decompression experiments. *Journal of Volcanology and Geothermal Research*, *161*(3), 151–164. https://doi.org/10.1016/j.jvolgeores.2006.12.001

Massol, H., & Koyaguchi, T. (2005). The effect of magma flow on nucleation of gas bubbles in a volcanic conduit. *Journal of Volcanology and Geothermal Research*, *143*(1-3), 69–88. https://doi.org/10.1016/j.jvolgeores.2004.09.011

Mourtada-Bonnefoi, C. C., & Laporte, D. (1999). Experimental study of homogeneous bubble nucleation in rhyolitic magmas. *Geophysical Research Letters*, *26*(23), 3505–3508. https://doi.org/10.1029/1999gl008368

Mourtada-Bonnefoi, C. C., & Laporte, D. (2002). Homogeneous bubble nucleation in rhyolitic magmas: An experimental study of the effect of H_2O and CO_2. *Journal of Geophysical Research*, *107*(B4), 2066. https://doi.org/10.1029/2001jb000290

Mourtada-Bonnefoi, C. C., & Laporte, D. (2004). Kinetics of bubble nucleation in a rhyolitic melt: An experimental study of the effect of ascent rate. *Earth and Planetary Science Letters*, *218*(3-4), 521–537. https://doi.org/10.1016/s0012-821x(03)00684-8

Murase, T., & McBirney, A. R. (1973). Properties of some common igneous rocks and their melts at high temperatures. *Geological Society of America Bulletin*, *84*(11), 3563–3592. https://doi.org/10.1130/0016-7606(1973)84<3563:POSCIR>2.0.CO;2

Navon, O., & Lyakhovsky, V. (1998). Vesiculation processes in silicic magmas. *Geological Society, London Special Publications*, *145*(1), 27–50. https://doi.org/10.1144/gsl.sp.1996.145.01.03

Nowak, M., Cichy, S. B., Botcharnikov, R. E., Walker, N., & Hurkuck, W. (2011). A new type of high-pressure low-flow metering valve for continuous decompression: First experimental results on degassing of rhyodacitic melts. *American Mineralogist*, *96*(8-9), 1373–1380. https://doi.org/10.2138/am.2011.3786

Ochs, F. A., & Lange, R. A. (1999). The density of hydrous magmatic liquids. *Science*, *283*(5406), 1314–1317. https://doi.org/10.1126/science.283.5406.1314

Piochi, M., Polacci, M., Astis, G. D., Zanetti, A., Mangiacapra, A., Vannucci, R., & Giordano, D. (2008). Texture and composition of pumices and scoriae from the Campi Flegrei caldera (Italy): Implications on the dynamics of explosive eruptions. *Geochemistry, Geophysics, Geosystems*, *9*, Q03013. https://doi.org/10.1029/2007gc001746

Plesset, M. S., & Prosperetti, A. (1977). Bubble dynamics and cavitation. *Annual Review of Fluid Mechanics*, *9*(1), 145–185. https://doi.org/10.1146/annurev.fl.09.010177.001045

Polacci, M. (2005). Constraining the dynamics of volcanic eruptions by characterization of pumice textures. *Annals of Geophysics*, *48*(4-5), 731–738.

Preuss, O., Marxer, H., Ulmer, S., Wolf, J., & Nowak, M. (2016). Degassing of hydrous trachytic Campi Flegrei and phonolitic Vesuvius melts: Experimental limitations and chances to study homogeneous bubble nucleation. *American Mineralogist*, *101*(4), 859–875. https://doi.org/10.2138/am-2016-5480

Prousevitch, A. A., Sahagian, D. L., & Anderson, A. T. (1993). Dynamics of diffusive bubble growth in magmas: Isothermal case. *Journal of Geophysical Research*, *98*(B12), 22,283–22,307. https://doi.org/10.1029/93jb02027

Randolph, A. D., & Larson, M. A. (1988). *Theory of particulate processes: Analysis and techniques of continuous crystallization*. Oxford, UK: Academic Press, Elsevier.

Sahagian, D. L., & Proussevitch, A. A. (1998). 3D particle size distributions from 2D observations: Stereology for natural applications. *Journal of Volcanology and Geothermal Research*, *84*(3-4), 173–196. https://doi.org/10.1016/s0377-0273(98)00043-2

Schmelzer, J. W. P., Abyzov, A. S., & Baidakov, V. G. (2017). Time of formation of the first supercritical nucleus, time-lag, and the steady-state nucleation rate. *International Journal of Applied Glass Science*, *8*(1), 48–60. https://doi.org/10.1111/ijag.12243

Schmelzer, J. W. P., & Baidakov, V. G. (2016). Comment on "Simple improvements to classical bubble nucleation models". *Physical Review E*, *94*, 026801. https://doi.org/10.1103/physreve.94.026801

Shea, T. (2017). Bubble nucleation in magmas: A dominantly heterogeneous process? *Journal of Volcanology and Geothermal Research*, *343*, 155–170. https://doi.org/10.1016/j.jvolgeores.2017.06.025

Sparks, R. S. J. (1978). The dynamics of bubble formation and growth in magmas: A review and analysis. *Journal of Volcanology and Geothermal Research*, *3*(1-2), 1–37. https://doi.org/10.1016/0377-0273(78)90002-1

Taniguchi, H. (1988). Surface tension of melts in the system $CaMgSi_2O_6$-$CaAl_2Si_2O_8$ and its structural significance. *Contributions to Mineralogy and Petrology*, *100*(4), 484–489. https://doi.org/10.1007/bf00371377

Tolman, R. C. (1949). The effect of droplet size on surface tension. *The Journal of Chemical Physics*, *17*(3), 333–337. https://doi.org/10.1063/1.1747247

Toramaru, A. (1989). Vesiculation process and bubble size distributions in ascending magmas with constant velocities. *Journal of Geophysical Research*, *94*(B12), 17,523–17,542. https://doi.org/10.1029/jb094ib12p17523

Toramaru, A. (1990). Measurement of bubble size distributions in vesiculated rocks with implications for quantitative estimation of eruption processes. *Journal of Volcanology and Geothermal Research*, *43*(1-4), 71–90. https://doi.org/10.1016/0377-0273(90)90045-h

Toramaru, A. (1995). Numerical study of nucleation and growth of bubbles in viscous magmas. *Journal of Geophysical Research*, *100*(B2), 1913–1931. https://doi.org/10.1029/94jb02775

Toramaru, A. (2001). A numerical experiment of crystallization for a binary eutectic system with application to igneous textures. *Journal of Geophysical Research*, *106*(B3), 4037–4060. https://doi.org/10.1029/2000JB900367

Toramaru, A. (2006). BND, (bubble number density) decompression rate meter for explosive volcanic eruptions. *Journal of Volcanology and Geothermal Research*, *154*(3-4), 303–316. https://doi.org/10.1016/j.jvolgeores.2006.03.027

Toramaru, A. (2014). On the second nucleation of bubbles in magmas under sudden decompression. *Earth and Planetary Science Letters*, *404*, 190–199. https://doi.org/10.1016/j.epsl.2014.07.035

Walker, D., & Mullins, O. (1981). Surface tension of natural silicate melts from 1200°–1500°C and implications for melt structure. *Contributions to Mineralogy and Petrology*, *76*(4), 455–462. https://doi.org/10.1007/bf00371487

Wallace, P. J., Plank, T., Edmonds, M., & Hauri, E. H. (2015). Chapter 7—Volatiles in magmas. In H. Sigurdsson (Ed.), *The encyclopedia of volcanoes* (2nd ed., pp. 163–183). Amsterdam: Academic Press. https://doi.org/10.1016/B978-0-12-385938-9.00007-9

Wilson, L., Sparks, R. S. J., & Walker, G. P. L. (1980). Explosive volcanic eruptions—IV. The control of magma properties and conduit geometry on eruption column behaviour. *Geophysical Journal International*, *63*(1), 117–148. https://doi.org/10.1111/j.1365-246x.1980.tb02613.x

Zhang, Y., & Behrens, H. (2000). H_2O diffusion in rhyolitic melts and glasses. *Chemical Geology*, *169*(1-2), 243–262. https://doi.org/10.1016/s0009-2541(99)00231-4

Zhang, Y., Belcher, R., Ihinger, P. D., Wang, L., Xu, Z., & Newman, S. (1997). New calibration of infrared measurement of dissolved water in rhyolitic glasses. *Geochimica et Cosmochimica Acta*, *61*(15), 3089–3100. https://doi.org/10.1016/s0016-7037(97)00151-8